Critical capillary waves of biomolecular condensates

Shunsuke F. Shimobayashi,[1,*] Kota Konishi,[1] Paul J. Ackerman,[2] Takashi Taniguchi,[3] and Clifford P. Brangwynne[2,4,†]

[1] *Center for iPS Cell Research and Application, Kyoto University, Sakyo-ku, Kyoto 606-8507, Japan*
[2] *Department of Chemical and Biological Engineering, Princeton University, Princeton, NJ 08544, USA*
[3] *Department of Chemical Engineering, Kyoto University, Kyoto 615-8510, Japan*
[4] *Howard Hughes Medical Institute, Princeton University, Princeton, NJ 08544, USA*

(Dated: August 19, 2023)

Membraneless compartments known as biomolecular condensates are thought to form through liquid-liquid phase separation (LLPS). When forces are applied to the fluid interfaces of these condensates, surface fluctuation are generated, a phenomenon known as capillary waves. The spatiotemporal dynamics of these fluctuations, characterized by the amplitude and velocity, reflect the physical properties of condensates. Moreover, unraveling the nature of fluctuations near the critical point is crucial for understanding the universal physical underpinnings of phase transitions. Although fluid condensate interfaces are ubiquitous within living cells, little is known about their surface fluctuations. Here, we quantify the interface fluctuations of light-induced synthetic and endogenous nuclear condensates, including nucleoli and nuclear speckles, in real and Fourier space. Measured fluctuations align with a theory assuming thermal driving, which enables measurement of surface tension and effective viscosity. The surface tensions fall within the range of 10^{-6} to 10^{-5} N/m for all tested condensates; in contrast, we find significant difference of fluctuation velocities, highlighting much higher viscosity of nucleoli $\sim 10^4$ Pa·s, compared to synthetic condensates and nuclear speckles. We further find that the interface fluctuations become enhanced and slower as the system nears the critical point. These findings elucidate key aspects of intracellular condensate properties, and suggest that the critical trend of surface tension is more consistent with theoretical predictions by the mean-field model than those by the 3D Ising model.

There is growing evidence that intracellular compartmentalization by membraneless organelles or biomolecular condensates is achieved through liquid–liquid phase separation [1–4]. These condensates are involved in various biological functions, including gene expression, RNA metabolism, DNA repair and signal transduction. Multivalent interactions mediated by RNA and proteins, particularly enriched in intrinsically ordered regions (IDRs), drive condensate formation. Condensate interfaces directly interact with other organelles, including cell membranes, chromatin and the cytoskeleton. These interfacial interactions cooperatively tune the morphologies, structures and biological functions, partly due to the mechanical forces acting through these interfaces, highlighting the importance of interfacial material properties.

When thermal forces are applied to fluid interfaces with relatively low surface tension, it can generate observable micron-scale fluctuations, as demonstrated by work on colloid-polymer solutions [5]. The spatiotemporal dynamics of surface fluctuations, called capillary waves, reflect the physical properties of the droplet surface. In the biological context, unraveling the nature of condensate fluctuations near the critical point is crucial for understanding the physical principles of intracellular phase separation. Although many condensates have been studied over the last decade, the biophysical properties of their interfaces, and the roles of interfacial fluctuations, remain elusive.

To quantify the interface properties of condensates in living cells, we first examine a tractable optogenetic system, Corelets [3, 6]. Corelets enable the control of phase separation through light-activated oligomerization of IDRs of proteins including FUS or HNRNPA1 (FUS_N, 1–214; $HNRNPA1_C$, 186–320), model aromatic-rich polar sequences in human osteosarcoma (U2OS) cells [3, 6] (Fig.1a). We activate optogenetic oligomerization and then record the time-lapse images of the resulting condensates and detect the contours (see methods), clearly observing surface fluctuations with a velocity of approximately 10 nm per sec (Fig.1b,c). We find that the time-averaged contours are generally not perfect circles (Fig.1b), likely due to the inhomogenous mechanical environment in living cells. In order to quantify the fluctuations, we consider the contour deviation $\delta r(\theta, \Delta t)$ with a time-lag Δt

$$\delta r(\theta, \Delta t) = r(\theta, t + \Delta t) - r(\theta, t), \tag{1}$$

where we set a polar coordinate system from the center of mass of each condensate. Fig.1d shows the ensemble average of fluctuation amplitude $\langle |\delta r(\Delta t)|^2 \rangle$ as a function of Δt, here $\langle\rangle$ represents an ensemble average. Through single exponential fitting $\langle |\delta r(\Delta t)|^2 \rangle \propto 1 - e^{-\Delta t/\Delta t_0}$, the relaxation time of fluctuations Δt_0 was found to be 2.6 ± 1.3 s and 1.1 ± 0.1 s for FUS_N and $HNRNPA1_C$-Corelets, respectively.

Fourier transformation of experimentally measured fluctuations $\langle |\delta r(\theta, \Delta t)|^2 \rangle$ yields the ensemble average of

* s.shimobayashi@cira.kyoto-u.ac.jp
† cbrangwy@princeton.edu

fluctuation spectrum, i.e., $\langle|\delta r(q_n,\Delta t)|^2\rangle$, where $q_n = n/r_0$ with mode number n and mean condensate radius r_0. Fig.1e represents the fluctuation spectrum $\langle|\delta r(q_n,\Delta t)|^2\rangle$ for a single condensate of $\mathrm{FUS_N}$ and $\mathrm{HNRNPA1_C}$-Corelets (500 frames, $\Delta t = 0.06, 0.3, 30$ sec). The spectrum monotonically increases from 10^{-6} to 10^{-5} $\mu\mathrm{m}^2$ as Δt increases and exhibits a power law with a slope of nearly -2 against q well above Δt_0, as also seen in spectra for a large set of individual $\mathrm{FUS_N}$ and $\mathrm{HNRNPA1_C}$ condensates (Fig.1f).

To theoretically elucidate the power-law behavior, we model the free energy functional of the condensate surfaces, which can be expressed as

$$F_1 = \gamma d \int_0^{2\pi} (r^2 + r_{,\theta}^2)^{1/2} d\theta + \frac{\kappa d}{2}\int_0^{2\pi} H^2 \sqrt{g} d\theta, \quad (2)$$

here γ, d, κ and H are condensate surface tension, condensate thickness, surface bending modulus, and surface local curvature defined as $H = (2r_{,\theta}^2 + r^2 - rr_{,\theta\theta})/g^{3/2}$, where $r_{,\theta} = \partial r/\partial\theta$ and $r_{,\theta\theta} = \partial^2 r/\partial\theta^2$. Moreover, the equation of motion of the condensate surface is described as $-\delta F_1/\delta r = \xi \partial r/\partial t$ (see methods), where ξ is the friction coefficient. Assuming thermally-driven surface fluctuations of incompressible condensates, $\langle|\delta r(q_n,\Delta t)|^2\rangle$ can be described as when $n \gg 1$,

$$\langle|\delta r(q_n,\Delta t)|^2\rangle = \frac{2(1-e^{-2e_q\Delta t/\xi})k_\mathrm{B}T}{e_q}, \quad (3)$$

$$e_q = \pi r_0 d(\gamma q^2 + \kappa q^4), \quad (4)$$

here k_B and T are the Boltzmann constant and temperature, respectively. Furthermore, when $\Delta t \to \infty$,

$$\langle|\delta r(q)|^2\rangle = \frac{2k_\mathrm{B}T}{\pi r_0 d(\gamma q^2 + \kappa q^4)}. \quad (5)$$

The parameters γ and κ can be measured by fitting the spectrum $\langle|\delta r(q_n,\Delta t)|^2\rangle$ with $\Delta t \gg \Delta t_0$ using equation (5), followed by determining the friction coefficient ξ by fitting $\langle|\delta r(q_n,\Delta t)|^2\rangle$ with $\Delta t < \Delta t_0$ using equation (3).

To validate the applicability of the framework to thermal systems, we numerically simulate the time evolution of a phase-separated condensate with Model B based on the Flory-Huggins mixing free energy (see methods). We observed the surface fluctuation which satisfies the fluctuation dissipation theorem [7] and exponential-type relaxation, similar to our experimental results (Fig. 1g and Extended Data Fig.1). Fig.1g represents the fluctuation spectrum $\langle|\widetilde{\delta r}(n,\widetilde{\delta t})|^2\rangle$ for a single condensate against n, where $\widetilde{\delta t}$ is the lag-time in simulation. Hereafter the tilde stands for dimensionless quantities in numerical simulations (see methods). Equations (3) and (5) well-fit the fluctuation spectrum $\langle|\widetilde{\delta r}(n,\widetilde{\delta t})|^2\rangle$, yielding $\widetilde{\gamma}$ and $\widetilde{\xi}$ (see the solid and dashed lines in Fig. 1g(ii)). Using the crossover parameter $q^* = n^*/r_0 = \sqrt{\xi/2\pi r_0 d\gamma\Delta t}$, equation (3) can be written as $\langle|\widetilde{\delta r}(n,\widetilde{\delta t})|^2\rangle = 2k_\mathrm{B}T(1 - e^{-(n/n^*)^2})/e_n$ Plotting n^{*2} for various $\widetilde{\delta t}$, $n^{*2}\widetilde{\delta t}$ aligns with a constant line, confirming that the friction coefficient is independent of time-lag $\widetilde{\delta t}$ (Extended Data Fig.2). Note that the bending modulus cannot be measured as $\langle|\widetilde{\delta r}(n,\widetilde{\delta t})|^2\rangle \not\propto n^{-4}$ even for high-n region; this suggests that interfacial bending rigidity does not contribute to the fluctuations, at least on experimentally observable length scales (Fig.1g).

Our findings that the spectrum $\langle|\delta r(q_n,\Delta t)|^2\rangle$ is well-described by these theoretical predictions suggest that these intracellular fluctuations are driven thermally, despite potential non-equilibrium driving forces within living cells. Thus, using equations (3) and (5), we can measure the surface tension γ and friction coefficient ξ, respectively (see the solid and dashed lines in Fig. 1e). Fig.1h presents a quantitative map of γ and ξ obtained from fitting the statistical data (16 and 23 condensates for $\mathrm{HNRNPA1_C}$ and $\mathrm{FUS_N}$-Corelets, respectively). The surface tension γ ranges from 10^{-6} to 10^{-5} N/m, in alignment with previously reported values for in vitro and vivo condensates [8–11], and ξ from 10^{-4} to 10^{-3} N·s/m. The variance of obtained parameters between cells is probably due to the difference in core-to-IDR ratio, f; the core-to-IDR ratio represents the degree of IDR oligomerization, (Fig. 3a) [3]. Additionally, a time quantity ξ/γ can be quantified through the linear fitting of ξ and γ (see the dashed line in Fig.1h), resulting in $\xi/\gamma \approx 100$ sec. Assuming that the slowest fluctuation with $n = 2$ dominates the fluctuation dynamics in real space, the relaxation time Δt_0 can be described as $\xi/2e_{q_2}$. Using $\xi/\gamma \approx 100$ sec and $r_0 \approx d$, Δt_0 can be obtained as on the order of 1 second, which is quantitatively consistent with our measurements in real space (Fig. 1d).

Next, we aimed to test the applicability of our approach for endogenous nuclear condensates, focusing on nucleoli, sites of ribosomal biogenesis [8, 9, 12], and nuclear speckles, storage areas for mRNA processing and splicing factors [13] (Fig.2a). As clearly shown in Fig.2b, we observed different magnitudes and characteristic time scales of interface fluctuations. We calculated the spectrum $\langle|\delta r(q_n,\Delta t)|^2\rangle$ with $\Delta t = 750$ sec for nuceloli and $\Delta t = 250$ sec for nuclear speckles, respectively, confirming a power law with the exponent -2, alongside larger fluctuation of nuclear speckles (Fig.2c). To check the experimental noise, excluding real surface fluctuations, we measured $\langle|\delta r(q_n,\Delta t)|^2\rangle$ with $\Delta t = 750$ sec for nuceloli and $\Delta t = 250$ sec for nuclear speckles after fixing the cells with 4 % paraformaldehyde (Extended Data Fig.3), confirming that the fluctuation signal is above the noise floor, particularly for large wavelength fluctuations (low q) (Fig.2c). We determined γ and ξ through the theoretical fitting of the spectrum with equations (3) and (5), displayed as a quantitative map in Fig.2d. As expected by larger fluctuations of nuclear speckles, the surface tension for nucleoli is five times larger than nuclear speckles and similar to those of corelet condensates. These values are comparable to those reported for nucleoli in HeLa cells and Xenopus oocytes [8, 9] and colloid-polymer solutions [5]. In contrast, we found that the friction co-

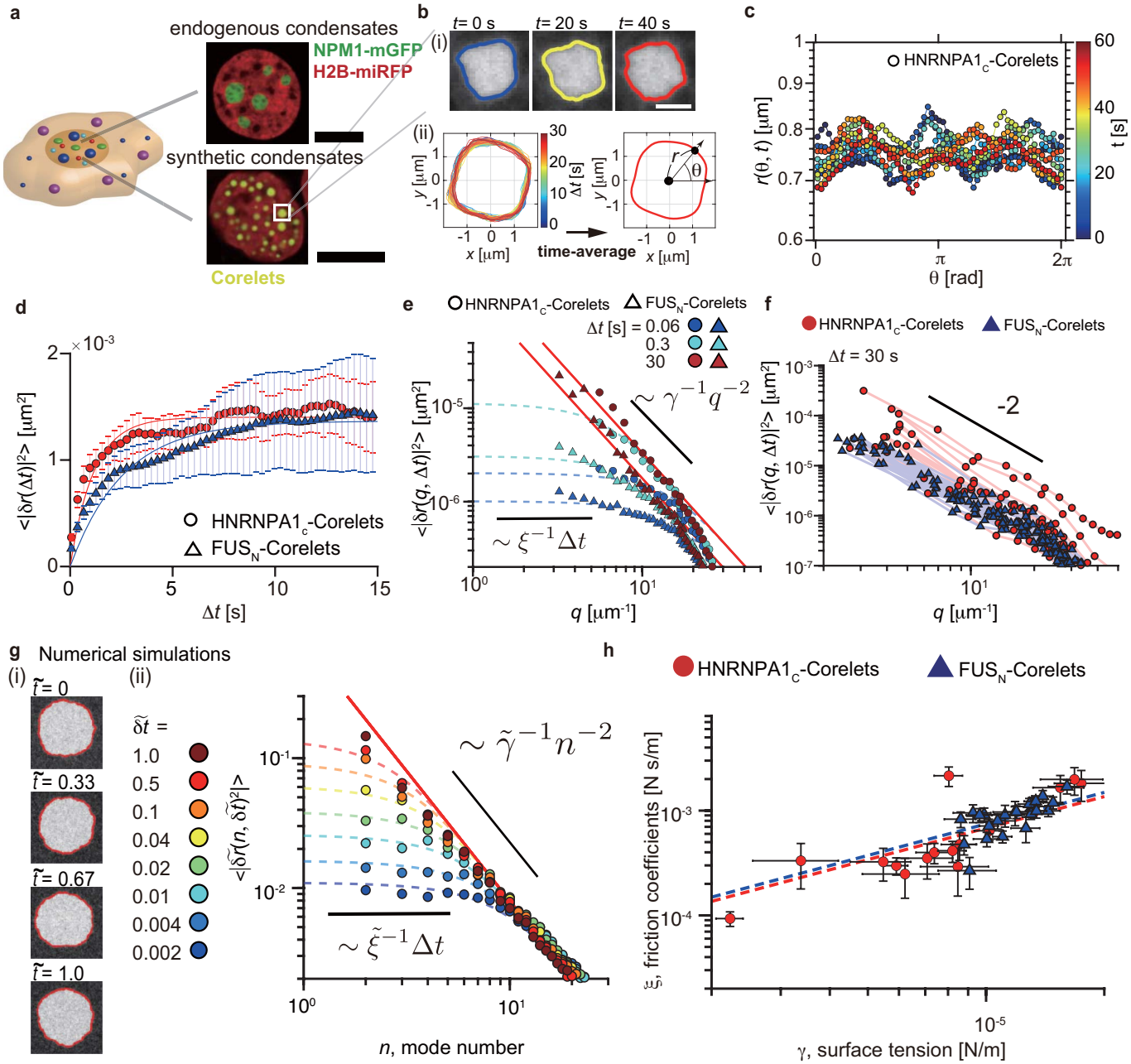

FIG. 1. Measuring surface fluctuations of biomolecular condensates in living cells. (a) Confocal fluorescence images of U2OS cells show nucleoli (NPM1-mGFP) and synthetic condensates (HNRNPA1$_{\mathrm{C}}$-Corelets). Scale bar, 10 μm. (b)(i) Surface fluctuation of HNRNPA1$_{\mathrm{C}}$-Corelets. The condensate interfaces are represented by the solid lines. Edge colours correspond to the time t. Scale bar, 1 μm. (ii) Overplots and time-average of contours of HNRNPA1$_{\mathrm{C}}$-Corelets over 30 sec with $\Delta t = 180$ ms (167 frames) (c) Temporal dynamics of condensate contour $r(\theta, t)$ for HNRNPA1$_{\mathrm{C}}$-Corelets ($t = 0, 12, 24, 36, 48, 60$ s). (d) Ensemble average of fluctuation amplitude $\langle|\delta r(\Delta t)|^2\rangle$ as a function of Δt for FUS$_{\mathrm{N}}$ and HNRNPA1$_{\mathrm{C}}$-Corelets. The solid lines show the best fit to $\langle|\delta r(\Delta t)|^2\rangle \propto 1 - e^{-\Delta t/\Delta t_0}$. (e) Fluctuation spectrum $\langle|\delta r(q, \Delta t)|^2\rangle$ of a single condensate against wave vector q with various $\Delta t (= 0.06, 0.3, 30$ s) for FUS$_{\mathrm{N}}$ and HNRNPA1$_{\mathrm{C}}$-Corelets. The dashed and solid lines represent the best fits to equations (3) and (5), respectively. (f) Fluctuation spectrum $\langle|\delta r(q, \Delta t)|^2\rangle$ against q with $\Delta t = 30$ s for FUS$_{\mathrm{N}}$ ($n = 23$) and HNRNPA1$_{\mathrm{C}}$ ($n = 16$)-Corelets. (g) (i) Surface fluctuation of numerically calculated condensates represented by the red solid lines. (ii) Fluctuation spectrum $\langle|\widetilde{\delta r}(n, \widetilde{\delta t})|^2\rangle$ against a mode number n with various time-lag $\widetilde{\delta t}$. The dashed and solid lines represent the best fits to equations (3) and (5). (h) Quantitative correlation between friction coefficients ξ and surface tension γ for FUS$_{\mathrm{N}}$ ($n = 23$) and HNRNPA1$_{\mathrm{C}}$ ($n = 16$)-Corelets. n is the number of analyzed condensates.

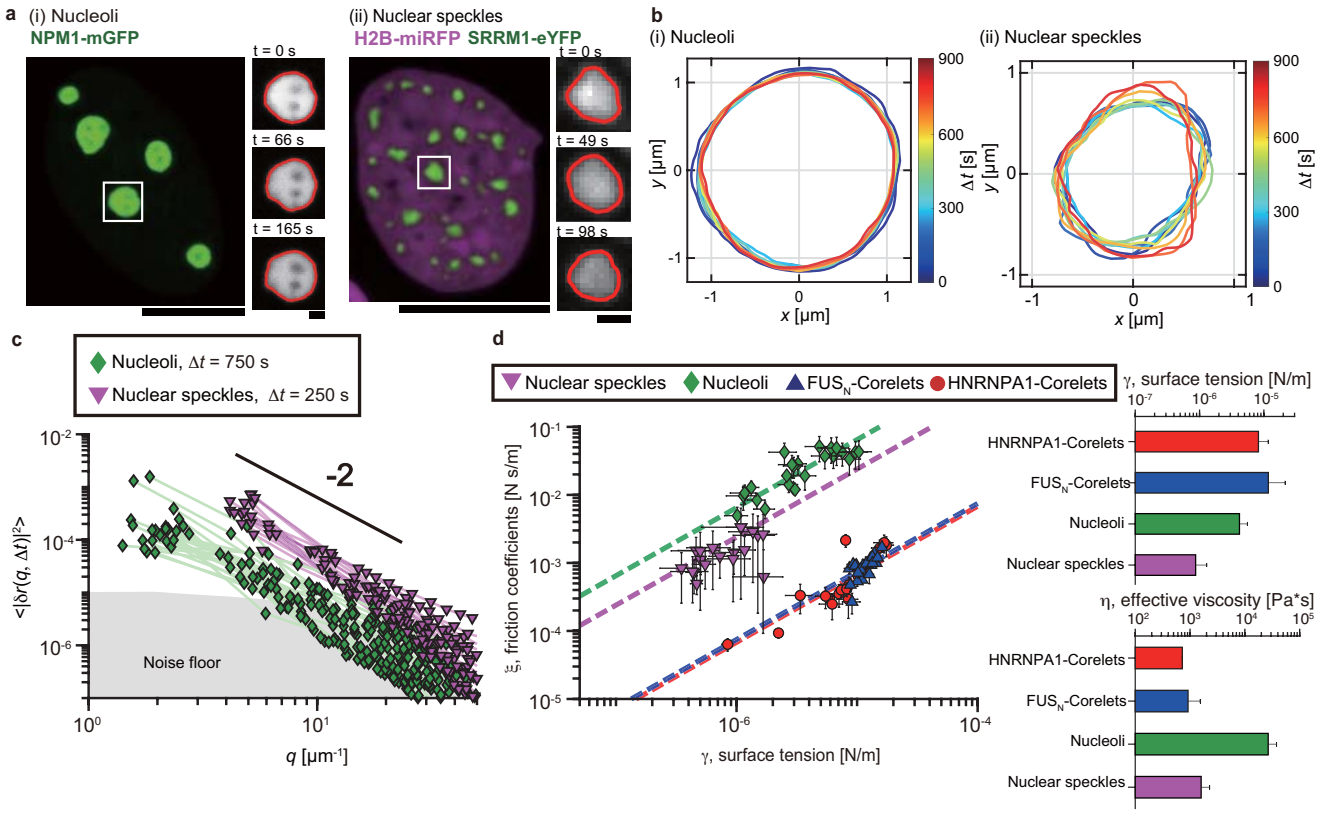

FIG. 2. Measuring surface fluctuations to probe material properties of endogenous condensates. (a) Fluorescence images of U2OS cells show nucleoli (NPM1-mGFP) and nuclear speckles (SRRM1-eYFP). Time-lapse confocal images of a single condensate are also displayed. (b) Overplots of a single condensate contour of (i) nucleoli and (ii) nuclear speckles in U2OS cells with (i) $\Delta t = 30$ s (50 frames) and (ii) $\Delta t = 10$ s (50 frames). (c) Fluctuation spectrum $\langle|\delta r(q,\Delta t)|^2\rangle$ against q with $\Delta t = 750$ sec for nucleoli ($n = 24$) and $\Delta t = 250$ sec for nuclear speckles ($n = 19$). (d) Quantitative correlation of friction coefficients ξ and surface tension γ for nucleoli ($n = 24$), nuclear speckles ($n = 19$), $\mathrm{FUS_N}$ ($n = 23$) and $\mathrm{HNRNPA1_C}$-Corelets ($n = 16$). (right) Bar graphs exhibit the mean and standard deviation for γ and η. Scale bar, 10 μm. n is the number of analyzed condensates.

efficient ξ is more than an order of magnitude larger for nucleoli compared to corelet condensates and nuclear speckles. The friction coefficient ξ is linked to the effective viscosity η as $\xi \approx \eta l$, with l representing the typical length-scale of fluctuations in real space. As l approximates the condensate size ≈ 1 μm, we can evaluate the effective viscosity, shown in a bar graph (Fig.2d). Given the reported viscosity of nucleoplasm, 10^2 to 10^3 Pa·s [14, 15], η can be interpreted as the viscosity of condensates. The viscosity of corelet condensates and nuclear speckles can be estimated to be within the range of an order of magnitude of 10^3 Pa·s. This is a thousand times higher than water droplets and most in vitro condensates (~ 1 Pa·s), illuminating sticky intracellular environments [10, 11]. Meanwhile, the viscosity for nucleoli is more than an order of magnitude larger than nuclear speckles, namely $\approx 10^4$ Pa·s, which is similar to that of nucleoli in Xenopus oocytes [8]. The high viscosity likely reflects the contributions from the elastic components of the condensates, described as $G\tau$, where G and τ are shear modulus and viscoelastic relaxation time, respectively [16], and could also reflect contributions from the surrounding viscoelastic environment.

To gain further physical insights into these material properties, we measure the critical behaviors of condensates using controllable optogenetics, i.e., Corelets, where we can quantitatively manipulate the position in a phase diagram by adjusting the laser power of blue light to control the binding of core and IDRs. As shown in Fig.3a, as the system approaches the critical point, namely, $f \to f_c$ (or equivalently, the Flory-Huggins parameter $\chi \to \chi_c$ and concentration ratio of dilute and dense phases $C_{\mathrm{dil}}/C_{\mathrm{den}} \to 1$), the Flory-Huggins model to describe polymer phase separation in inanimate systems predicts surface tension γ vanishes at this point [17]. By weakening the light intensity to bring a cell closer to the critical point ($C_{\mathrm{dil}}/C_{\mathrm{den}} \to 1$), we observed a significant increase in surface fluctuations (Fig.3b,c), as expected from theory [17]. Moreover, we also found slower dynamics of condensate fusion (Fig.3d), indicating the occurrence of critical slowing down [17]. By fitting the spectrum $\langle|\delta r(q_n,\Delta t)|^2\rangle$ using equation (5), we es-

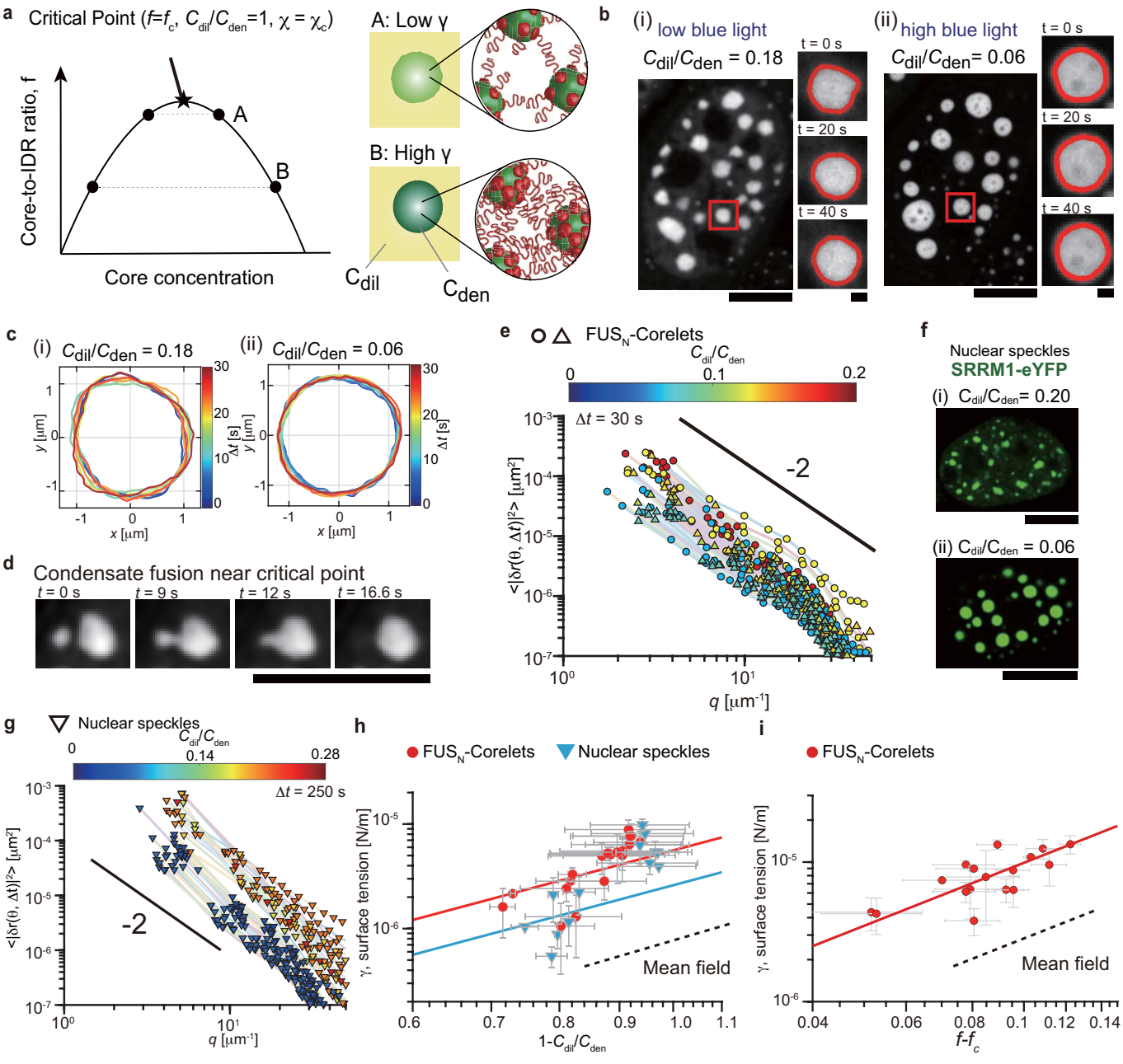

FIG. 3. Critical capillary waves of synthetic and endogenous condensates. (a) Schematic of a phase diagram of Corelet system shows that surface tension γ decreases as a cell approaches the critical point, where $f = f_c$, $\chi = \chi_c$ and $C_{\rm dil}/C_{\rm den} = 1$. (b) Fluorescence images of U2OS cells expressing $\rm FUS_N$-Corelets subjected to approximately (i) 10^{-4} W/cm^2 and (ii) 10^{-2} W/cm^2 intensities of blue light. Scale bar, 10 μm. Time-lapse confocal images of a single condensate are also displayed. Scale bar, 1 μm. (c) Overplots of single condensate contours in U2OS cells expressing $\rm FUS_N$-corelets under approximately (i) 10^{-4} W/cm^2 and (ii) 10^{-2} W/cm^2 intensities of blue light with $\Delta t = 180$ ms over 30 sec. (d) A droplet fusion of $\rm FUS_N$-corelet condenates in a U2OS cell near the critical point. (e) Fluctuation spectrum $\langle|\delta r(q, \Delta t)|^2\rangle$ against q with $\Delta t = 30$ s and various ratios $C_{\rm dil}/C_{\rm den}$ for U2OS cells expressing $\rm FUS_N$-Corelets ($n = 60$). (f) Fluorescence images of U2OS cells expressing different levels of SRRM1-eYFP. (g) Fluctuation spectrum $\langle|\delta r(q, \Delta t)|^2\rangle$ of U2OS cells expressing various levels of SRRM1-eYFP with $\Delta t = 250$ s and various ratios $C_{\rm dil}/C_{\rm den}$ against q (49 condensates, 13 cells). (h) Surface tension γ against $1 - C_{\rm dil}/C_{\rm den}$ for $\rm FUS_N$-Corelets (103 condensates, 19 cells) and nuclear speckles (49 condensates, 13 cells). The data points and error bars show the mean and standard deviation in single cells. The solid and dashed lines show the theoretical prediction $\gamma \propto (1 - C_{\rm dil}/C_{\rm den})^{6\beta}$ by the mean-field model ($\beta = 1/2$). (i) Surface tension γ against $f - f_c$ for $\rm FUS_N$-Corelets (n=16, 4 cells). The solid line shows the best fit to the equation $\gamma \propto (f - f_c)^{3\beta}$ ($\beta = 1/2$).

timated γ for various $C_{\rm dil}/C_{\rm den}$ ratios, confirming that the spectrum $\langle|\delta r(q_n,\Delta t)|^2\rangle$ increases with the increase in $C_{\rm dil}/C_{\rm den}$ so that γ decreases (Fig. 3e). This trend quantitatively aligns with the theoretical prediction derived from the expansion of the Flory-Huggins model near the critical point, namely $\gamma \propto (1 - C_{\rm dil}/C_{\rm den})^{6\beta}$ ($\beta = 1/2$, see Fig. 3h and reduced chi-squared values of model fitting $\chi^2_{\rm red}$ in Extended Data Fig.4a). Moreover, plotting γ against $f - f_c$ also confirmed the prediction, i.e., $\gamma \propto (f - f_c)^{3\beta}$ ($\beta = 1/2$, see $\chi^2_{\rm red}$ in Extended Data Fig.4b), where we used the value $f_c = 0.18\pm0.02$ from [3]. The consistency with the Flory-Huggins model thus falls into the mean-field universality class; however, we do not necessarily exclude the 3D Ising model ($\beta = 0.326$). For further investigation of the critical capillary waves in endogenous condensates, we overexpressed SRRM1, a key scaffold protein of nuclear speckles, significantly beyond its native levels, leading to speckles becoming more spherical, a decrease in the concentration ratio $C_{\rm dil}/C_{\rm den}$, and diminished fluctuations (Fig.3 f,g). This results in an increase in surface tension, likely due to the increased distance from the critical point. Despite the complex nature of endogenous condensates, the obtained surface tension was found to have similar values and dependence on proximity to the critical point (Fig.3h, see $\chi^2_{\rm red}$ in Extended Data Fig.4c). The surface tension for synthetic and endogenous condensates quantitatively demonstrates the critical phenomena, more consistent with the mean-field universality class than 3D Ising model [17]. This is in contrast to membrane phase separation, where the Ising universality class was found [18]. This highlights the potential difference between the underlying physical basis of intracellular phase separation driven by RNA-protein or lipids, possibly due to the polymer properties of RNA/proteins. Regarding nuclear speckles, the observation of larger fluctuations when the expression levels of SRRM1 are close to native levels suggests that the endogenous system is near a critical point. This can lead to more long-range fluctuations in concentration, which might play a role in the transmission of information and materials within the intracellular space.

In conclusion, we measure sub-micron scale surface fluctuations to quantify surface tension and effective viscosity of intracellular synthetic and endogenous condensates in a non-invasive manner. The measured surface tension values range from 10^{-6} to 10^{-5} N/m, which is consistent with previously reported values for nucleoli in HeLa cells and Xenopus oocytes, and some in vitro condensates [8–10]. Surface fluctuations of nucleoli yield a remarkable high viscosity $\sim 10^4$ Pa·s, which is more than an order of magnitude larger than to corelet condensates and nuclear speckles. Considering that the nucleoplasm viscosity is around 10^2 to 10^3 Pa·s [14, 15], the condensate viscosity should govern the fluctuation dynamics. We further confirmed critical surface fluctuations as the system nears the critical point. The critical behaviors are quantitatively more consistent with theoretical predictions by the mean-field model than by 3D Ising one, illuminating the fundamental physical principles of intracellular phase separation. Given that the material properties of biomolecular condensates reflect their biological and pathological functions [19], our framework on the fluctuation analysis has the potential to pave the way for novel approaches in the diagnosis and drug development for the related diseases.

[1] Brangwynne, C. P. *et al.* Germline p granules are liquid droplets that localize by controlled dissolution/condensation. *Science* **324**, 1729–1732 (2009).

[2] Wei, M.-T. *et al.* Nucleated transcriptional condensates amplify gene expression. *Nat. Cell Biol.* **22**, 1187–1196 (2020).

[3] Shimobayashi, S. F., Ronceray, P., Sanders, D. W., Haataja, M. P. & Brangwynne, C. P. Nucleation landscape of biomolecular condensates. *Nature* **599**, 503–506 (2021).

[4] Su, X. *et al.* Phase separation of signaling molecules promotes t cell receptor signal transduction. *Science* **352**, 595–599 (2016).

[5] Aarts, D. G., Schmidt, M. & Lekkerkerker, H. N. Direct visual observation of thermal capillary waves. *Science* **304**, 847–850 (2004).

[6] Bracha, D. *et al.* Mapping local and global liquid phase behavior in living cells using photo-oligomerizable seeds. *Cell* **175**, 1467–1480 (2018).

[7] Shimobayashi, S. F., Ichikawa, M. & Taniguchi, T. Direct observations of transition dynamics from macro- to micro-phase separation in asymmetric lipid bilayers induced by externally added glycolipids. *EPL* **113**, 56005 (2016).

[8] Brangwynne, C. P., Mitchison, T. J. & Hyman, A. A. Active liquid-like behavior of nucleoli determines their size and shape in xenopus laevis oocytes. *Proc. Natl. Acad. Sci. U.S.A.* **108**, 4334–4339 (2011).

[9] Caragine, C. M., Haley, S. C. & Zidovska, A. Surface fluctuations and coalescence of nucleolar droplets in the human cell nucleus. *Phys. Rev. Lett.* **121**, 148101 (2018).

[10] Wang, H., Kelley, F. M., Milovanovic, D., Schuster, B. S. & Shi, Z. Surface tension and viscosity of protein condensates quantified by micropipette aspiration. *Biophys. Rep.* **1**, 100011 (2021).

[11] Jawerth, L. M. *et al.* Salt-dependent rheology and surface tension of protein condensates using optical traps. *Phys. Rev. Lett.* **121**, 258101 (2018).

[12] Feric, M. *et al.* Coexisting liquid phases underlie nucleolar subcompartments. *Cell* **165**, 1686–1697 (2016).

[13] Lamond, A. I. & Spector, D. L. Nuclear speckles: a model for nuclear organelles. *Nat. Rev. Mol. Cell Biol.* **4**, 605–612 (2003).

[14] Celedon, A., Hale, C. M. & Wirtz, D. Magnetic manipulation of nanorods in the nucleus of living cells. *Biophys. J.* **101**, 1880–1886 (2011).

[15] De Vries, A. H., Krenn, B. E., Van Driel, R., Subramaniam, V. & Kanger, J. S. Direct observation of nanomechanical properties of chromatin in living cells. *Nano Lett.* **7**, 1424–1427 (2007).

[16] Larson, R. G. *Constitutive equations for polymer melts and solutions: Butterworths series in chemical engineering* (Butterworth-Heinemann, 2013).

[17] Hohenberg, P. C. & Halperin, B. I. Theory of dynamic critical phenomena. *Rev. Mod. Phys.* **49**, 435–479 (1977).

[18] Veatch, S. L. *et al.* Critical fluctuations in plasma membrane vesicles. *ACS Chem. Biol.* **3**, 287–293 (2008).

[19] Lafontaine, D. L., Riback, J. A., Bascetin, R. & Brangwynne, C. P. The nucleolus as a multiphase liquid condensate. *Nature reviews Molecular cell biology* **22**, 165–182 (2021).

METHODS

Cell culture

Human cell lines used in this study include U2OS and Lenti-X 293T (Takara Bio USA). Lenti-X 293T cells were only used for virus production, while U2OS cells were used for experiments. Cells were cultured in growth medium (DMEM, Nacalai) supplemented with 10% FBS (Wako) and penicillin and streptomycin (Nacalai) at 37°C with 5% CO2 in a humidified incubator.

Plasmid construction

Plasmids were transformed into Stellar cells (Clontech), from which single colonies were picked, grown in LB supplemented by Ampicillin for 16 hours, and miniprepped (QIAGEN) following manufacturer instruction. All cloning products were confirmed by sequencing (GENEWIZ). The constructs (pHR-FUS_N-mCherry-sspb, pHR-$HNRNPA1_C$-mCherry-sspb, pHR-NLS-iLID-EGFP-FTH1, FM5-NPM1-GFP, pHR-H2B-miRFP670, pHR-mGFP-P2A-mCherry, FM5-SRRM1-eYFP) are derived from those used in our previous studies [3, 6].

Lentiviral transduction

Lentiviruses were produced by cotransfecting Lenti-X 293T cells grown to approximately 70% confluency, controlled with Countess 3 FL (Thermo), in 6-well plates with transfer plasmids (1.5 µg), pCMV-dR8.91 (1.33 µg) and pMD2.G (0.17 µg) using FuGENE HD Transfection Reagent (Promega) following manufacturer's instruction. After 2 days, 2 mL of supernatant containing viral particles was harvested and filtered with 0.45 µm filter (Merck). Supernatant was immediately used for transduction or stored at -80℃ in aliquots.

Construction of stable cell lines

U2OS cells were grown to 10-20% confluency, controlled with Countess 3 FL (Thermo), on 96 well glass-bottom dishes (Cellvis) and 10-100 µl of filtered viral supernatant was added to the cells. Virus-containing medium was replaced with fresh growth medium 48 hours post-infection. The cells were typically imaged no earlier than 72 hr after infection.

Corelets (Core scaffolds to promote droplets)

Corelets have a two-module optogenetic system that mimics the endogenous oligomerization of IDR-rich proteins to drive biomolecular condensation, using a light-activatable high valency core [3, 6]. The core is comprised of 24 human ferritin heavy chain (FTH1) protein subunits, which self-assemble to form a spherical particle of 12 nm diameter (referred to as "Core"), which is fused to a nuclear localization signal (NLS) and an engineered protein iLID. The second module is comprised of a self-interacting IDR fused to SspB, which upon blue light activation strongly heterodimerize ($K_d \sim 130$ nM) with iLID to form self-interacting particles.

Cell fixing

U2OS Cells stably expressing NPM1-mGFP were fixed with 4% paraformaldehyde (Nacalai) in PBS (Nacalai) and incubated for 12 min at room temperature, followed by three times rinse with PBS.

Microscopy

Fluorescence images were taken using a spinning-disk confocal microscope (Yokokgawa CSU-W1) with Nikon 100x oil immersion objective (CFI Plan Apo λD, NA 1.45) and an Andor iXon Ultra 888 EMCCD camera on a Nikon Eclipse Ti2-E body. Samples were maintained at 37℃ and 5% CO2 with a stage top incubator (Tokai Hit). 488, 561, and 640 nm lasers (Stradus) were used for imaging mGFP/eYFP, mCherry, and miRFP, respectively. 488 nm laser light was also used for activating iLID at an excitation power of approximately 10^{-4} to 10^{-2} W/cm^2 as measured with a microscope slide photodiode power sensor (PM100D, Thorlabs). Phase separation dynamics for the Corelet system were captured by imaging in mCherry channel with global activation by 488 nm laser. All image acquisition was performed using Nikon NIS-Elements AR software. All image analysis was performed using custom-built Python and MATLAB scripts (The Math Works).

Numerical simulation of phase separation: Model B

The condensate surface fluctuation is numerically calculated using Model B [17]. The free energy functional of phase separation is expressed as F_2

$$F_2 = \frac{k_{\rm B}T}{a^2}\int\left[\frac{\xi_0^2}{2}(\triangledown\phi)^2 + f(\phi)\right]dxdy, \tag{6}$$

where F is the Ginzburg-Landau free energy at temperature T, and $k_{\rm B}$ is the Boltzmann constant, a denotes the unit cell length, and ξ_0 is the correlation length. The potential $f(\phi)$ is $a_2\phi^2/2 + a_4\phi^4/4$, where a_2 and a_4 are the negative and positive coefficients, respectively. The temporal dynamics of $\phi(x, y, t)$ follow the continuity equation.

$$\frac{\partial\phi}{\partial t} + \nabla\cdot\boldsymbol{j} = 0, \tag{7}$$

here, $\boldsymbol{j}$ is the total flux. The α-component $j_\alpha(\alpha = x, y)$ of $\boldsymbol{j}$ is the sum of thermodynamic fluxes by the gradients of chemical potential $\mu(x, y, t)$ and random current, $j_\alpha^{(r)}$, which can be represented as

$$j_\alpha = -L\partial\mu/\partial\alpha + j_\alpha^{(r)}, \tag{8}$$

here, L is the transport coefficient. The chemical potential μ, expressed as $\delta F_2/\delta\phi$, is calculated as follows:

$$\mu = \frac{k_{\rm B}T}{a^2}\Big[-\xi_0^2\nabla^2\phi + f'\Big], \tag{9}$$

where $f' = \partial f/\partial\phi$. The random current $j_\alpha^{(r)}$ satisfies the fluctuation dissipation theorem [7];

$$< j_\alpha^{(r)}(\boldsymbol{r}, t)j_\beta^{(r)}(\boldsymbol{r'}, t') >= 2k_{\rm B}TL\delta_{\alpha\beta}\delta(\boldsymbol{r}-\boldsymbol{r'})\delta(\boldsymbol{t}-\boldsymbol{t'}). \tag{10}$$

The phase separation dynamics can be described as

$$\frac{\partial\phi}{\partial t} = L\nabla^2\mu - \nabla\cdot\boldsymbol{j}^{(r)}. \tag{11}$$

In our simulations, space, time, and energy are scaled by Λ, τ_0, and ε_0, respectively, where $\Lambda^2 = \xi_0^2/|a_2|$, $\tau_0 = a\Lambda^2/k_{\rm B}TL|a_2|$, and $\varepsilon_0 = |a_2|\phi_{\rm eq}^2 k_{\rm B}T\Lambda^2/a$, with dimension d and $\phi_{\rm eq}$ defined as $\sqrt{|a_2|/a_4}$. This non-dimensionalization procedure yields time $\widetilde{t} = t/\tau_0$, time increment $\widetilde{\delta t} = \delta t/\tau_0$, and the strength of the random current $\widetilde{\eta} = \sqrt{2(a/\Lambda)/|a_2|}/\phi_{\rm eq}$ and time increment, where $\widetilde{\eta} = 0.5$ in this simulation.

To account for the effect of the length of constituent molecules, $f(\phi)$ can be expressed by Flory-Huggins mixing free energy :

$$f_{\rm FH}(\psi_{\rm A}, \psi_{\rm B}) = \frac{1}{N_{\rm A}}\psi_{\rm A}\ln\psi_{\rm A}\frac{1}{N_{\rm B}}\psi_{\rm B}\ln\psi_{\rm B} + \chi\psi_{\rm A}\psi_{\rm B} \tag{12}$$

where ϕ_α is the volume fraction of α-component ($\alpha \in \{{\rm A}, {\rm B}\}$) and satisfies $\psi_{\rm A} + \psi_{\rm B} = 1$ because of incompressiblity condition. The order parameter ϕ in equation (6) is related to ψ_α through the equation $\phi = \psi_{\rm A} - \psi_{\rm B}$. In the vicinity of the critical point, $f_{\rm FH}$ turns out to be the expression of $f(\phi)$ with $a_2 = 2(\chi_{\rm c} - \chi)$ and $a_4 = \frac{1}{3}\frac{(\sqrt{N_{\rm A}}+\sqrt{N_{\rm B}})^4}{(\sqrt{N_{\rm A}N_{\rm B}})^3}$, where $\chi_{\rm c} = \frac{1}{2}(\frac{\sqrt{N_{\rm A}}+\sqrt{N_{\rm B}}}{\sqrt{N_{\rm A}N_{\rm B}}})^2$.

Fluctuation analysis of condensate surface

To detect experimental and numerical condensate interface, we consider a polar coordinate system (R, θ) from the center mass of a condensate. The angle θ is then discretized by N points separated by a constant angle $\Delta\theta(= 2\pi/N)$. The camera-pixel based intensity profile was transformed to the discretized polar coordinate system using interp2 function in MATALB. The condensate contour $r_i(\theta_i, i = 1, ..., N)$ was measured as the crossing of a global intensity threshold with a sub-pixel resolution using a linear interpolation.

As shown in Fig.1b, the time-averaged shape of the condensate interface cannot be a perfect circle. So, we consider the contour difference with a time-lag $\delta r(\theta, \Delta t) = r(\theta, t + \Delta t) - r(\theta, t)$. Following the Fourier theory, $\delta r(\theta, \Delta t)$ can be described using the following series;

$$\delta r(\theta_{\rm m}, \Delta t) = \sum_{n=0}^{N-1}\delta r(n, \Delta t)e^{in\theta_{\rm m}}, \tag{13}$$

here, $\theta_{\rm m} = 2\pi/N$. The fluctuation spectrum can be represented as

$$\delta r(n, \Delta t) = \frac{1}{N}\sum_{m=0}^{N-1}\delta r(\theta_{\rm m}, \Delta t)e^{-in\theta_{\rm m}}, \tag{14}$$

which is calculated from experimentally measured $\delta r(\theta_{\rm m}, \Delta t)$ using MATLAB Fast Fourier Transform algorithm. An ensemble average of the fluctuation spectrum $\langle|\delta r(q_n, \Delta t)|^2\rangle$ is calculated as

$$\langle|\delta r(q_n, \Delta t)|\rangle^2 = \frac{1}{M}\sum_{j=1}^{M}|\delta r_j(q_n, \Delta t)|^2, \qquad (15)$$

here, M is the ensemble size and $q_n = n/r_0$. The parameter r_0 is defined by $r_0 = \sqrt{v_0/\pi d}$ with a constant volume v_0 due to the incompressibility and condensate thickness d.

Free energy of condensate surface

We consider the surface fluctuations of incompressible condensates with a thickness of d. Here, we assume negligible small fluctuations along the thickness. Following the Fourier theory, the condensate contour $r(\theta, t)$ can be described as;

$$r(\theta, t) = r_0 + R(\theta, t), \qquad (16)$$

$$R(\theta, t) = 2\sum_{n=1}^{\infty} C_n(t)e^{in\theta} \qquad (17)$$

Here, $C_n(t)$ is Fourier coefficient. The free energy functional of bending condensate interface is expressed as F_1

$$F_1 = \gamma d\int_0^{2\pi}(r^2 + r_{,\theta}^2)^{1/2}d\theta + \frac{\kappa d}{2}\int_0^{2\pi} H^2\sqrt{g}d\theta, \qquad (18)$$

here γ is condensate surface tension, $r_{,\theta} = \partial r/\partial\theta$, $r_{,\theta\theta} = \partial^2 r/\partial\theta^2$, κ is surface bending modulus, $H = (2r_{,\theta}^2 + r^2 - rr_{,\theta\theta})/g^{3/2}$, and $g = r^2 + r_{,\theta}^2$. Substituting equations (16) and (17) for equation (18), $\Delta F_1 = F_1 - 2\pi d(r_0\gamma + \kappa/r_0)$ can described as;

$$\Delta F_1 = 2\sum_{n=2}^{\infty}|C_n(t)|^2 e_n, \qquad (19)$$

$$e_n = \frac{\pi d}{r_0}\left[\gamma(n^2-1) + \frac{\kappa}{r_0^2}(n^4 - \frac{5}{2}n^2 + \frac{3}{2})\right]. \qquad (20)$$

The Boltzmann factor can be expressed as

$$P(\{C_n\}) = \exp\big(-\frac{\Delta F_1}{k_{\rm B}T}\big), \qquad (21)$$

here, $k_{\rm B}$ and T are the Boltzmann constant and temperature, respectively.

Equation of motion of condensate surface

The equation of motion of condensate surface can expressed as;

$$\xi\frac{\partial r(\theta, t)}{\partial t} = -\frac{\delta F_1}{\delta r}, \qquad (22)$$

where ξ is friction coefficient. Considering the first order contribution of R, equation(22) can be described as;

$$\frac{\partial R(\theta, t)}{\partial t} = -\frac{1}{\xi}\Big\{\frac{\partial}{\partial R}\Big(\frac{\delta F_1}{\delta R}\Big)\Big\}R. \qquad (23)$$

As the fluctuation of each mode can be treated as independent, equation (23) is written as using equations (17), (19) and (20);

$$\frac{dC_n(t)}{dt} = -\Gamma_n C_n(t), \qquad (24)$$

where

$$\Gamma_n = \frac{2e_n}{\xi}. \qquad (25)$$

Theoretical predictions of fluctuation spectrum

To theoretically predict the fluctuation spectrum $\langle|\delta r(q_n, \Delta t)|^2\rangle$, we define the following Fourier transformation;

$$\delta r(q_n, \Delta t) = \frac{1}{2\pi}\int_0^{2\pi}\delta r(\theta, \Delta t)e^{-in\theta}d\theta, \qquad (26)$$

$$\delta r(\theta, \Delta t) = \sum_{n=-\infty}^{\infty}\delta r(q_n, \Delta t)e^{in\theta}. \qquad (27)$$

From equation (27), the angular correlation function $\langle\delta r(\theta, \Delta t)\delta r(\theta', \Delta t)\rangle$ is described as,

$$\langle\delta r(\theta, \Delta t)\delta r(\theta', \Delta t)\rangle = \sum_{n=-\infty}^{\infty}\langle|\delta r(q_n, \Delta t)|^2\rangle e^{in(\theta-\theta')}, \qquad (28)$$

where we can assume that $\langle\delta r(\theta, \Delta t)\delta r(\theta', \Delta t)\rangle$ is a function of $\theta - \theta'$. Also, $\langle\delta r(\theta, \Delta t)\delta r(\theta', \Delta t)\rangle$ is obtained from equation(16) as;

$$\langle\delta r(\theta, \Delta t)\delta r(\theta', \Delta t)\rangle = \langle(R(\theta, \Delta t) - R(\theta, 0))(R(\theta', \Delta t) - R(\theta', 0))\rangle. \qquad (29)$$

Substituting equations (17) and (24) for equation (29),

$$\langle\delta r(\theta, \Delta t)\delta r(\theta', \Delta t)\rangle = \sum_{n=-\infty}^{\infty} 2(1 - e^{-\Gamma_n\Delta t})\langle|C_n(0)|^2\rangle e^{in(\theta-\theta')} \qquad (30)$$

where

$$C_n(\Delta t) = e^{-\Gamma_n\Delta t}C_n(0). \qquad (31)$$

From equations (28) and (30),

$$\langle|\delta r(q_n, \Delta t)|^2\rangle = 2(1 - e^{-\Gamma_n\Delta t})\langle|C_n(0)|^2\rangle. \qquad (32)$$

From equations (19-21),

$$\langle |C_n(0)|^2 \rangle = \frac{k_\mathrm{B}T}{e_n}. \tag{33}$$

Finally, when $n \gg 1$,

$$\langle |\delta r(q_n, \Delta t)|^2 \rangle = \frac{2(1 - e^{-2e_q \Delta t/\xi})k_\mathrm{B}T}{e_q}, \tag{34}$$

$$e_q = \pi r_0 d(\gamma q^2 + \kappa q^4) \tag{35}$$

, where $n = r_0 q_n$. So, when $\Delta t \to \infty$,

$$\langle |\delta r(q)|^2 \rangle = \frac{2k_\mathrm{B}T}{\pi r_0 d(\gamma q^2 + \kappa q^4)}. \tag{36}$$

The parameters γ and κ can be measured by fitting the spectrum $\langle |\delta r(q_n, \Delta t)|^2 \rangle$ with $\Delta t \gg \Delta t_0$ with equation (36), followed by determining the friction coefficient ξ by fitting $\langle |\delta r(q_n, \Delta t)|^2 \rangle$ with $\Delta t < \Delta t_0$ with equation (35).

Quantification of relaxation time of surface fluctuations

To quantify the relaxation time t_0, the fluctuation amplitude $\langle |\delta r(\theta, \Delta t)|^2 \rangle$ was first averaged over θ to obtain $\langle |\delta r(\Delta t)|^2 \rangle$. Through single exponential fitting $\langle |\delta r(\Delta t)|^2 \rangle \propto 1 - e^{-\Delta t/\Delta t_0}$, the relaxation time of fluctuation Δt_0 was obtained. For Fig. 1d, the data points and error bars show the mean and standard deviation, respectively.

Quantification of concentration ratio

To quantify the concentration ratio of the dilute and dense phases in the nucleus $C_\mathrm{dil}/C_\mathrm{den}$ after phase separation in the steady state, the condensates were automatically segmented by a single intensity threshold based on the bimodal fluorescent histogram of core component or SRRM1-eYFP within the segmented nucleus. To accurately determine the concentration, morphological erosion and dilation were performed for the segmentated condensates, such that three pixels (≈ 0.48 μm) near the condensate interface were excluded from the analysis. The concentration ratio $C_\mathrm{dil}/C_\mathrm{den}$ were estimated from the average fluorescence intensities of the background-subtracted image in the segmentated dilute and dense regions.

AUTHOR CONTRIBUTIONS

S.F.S., T.T. and C.P.B. designed the research; S.F.S. and P.J.A. developed the analysis codes; S.F.S. and K. K. performed the experiments; T.T. performed numerical simulations; S.F.S. analyzed the experimental and numerical data; S.F.S. wrote the manuscript; S.F.S, P.J.A., T.T., and C.P.B. reviewed and edited the draft.

ACKNOWLEDGMENTS

We wish to acknowledge Akira Miyaki, Nguyen Thai Le and Dr. Tomo Kurimura for experimental and analytical support. This work was supported in parts by JST, PRESTO Grant Number JPMJPR21E8 (to S.F.S.), Japan, JSPS KAKENHI Grant Numbers 18K13521, 23K13072 (to S.F.S.), research grants from iPS Cell Research Fund (to S.F.S.), the Uehara Memorial Foundation (to S.F.S.), Nakatani foundation (to S.F.S.), The Kao Foundation for Arts and Sciences (to S.F.S.), 2022 iPS Academia Japan Grant (to S.F.S.), AFOSR MURI grant (to C.P.B.), and Princeton MRSEC (to C.P.B.).

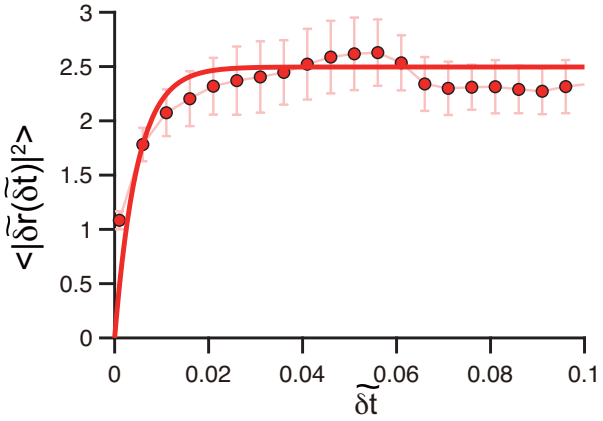

FIG. ED1. Relaxation dynamics of fluctuation. Ensemble average of fluctuation amplitude $\langle|\widetilde{\delta r}(n,\widetilde{\delta t})|^2\rangle$ as a function of $\widetilde{\delta t}$. The solid line shows the best fit to $\langle|\widetilde{\delta r}(n,\widetilde{\delta t})|^2\rangle \propto 1 - e^{-\widetilde{\delta t}/\widetilde{\delta t_0}}$.

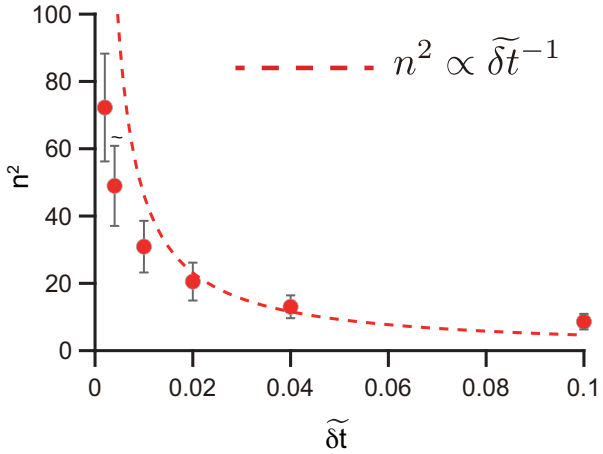

FIG. ED2. Square of mode number n^2 against $\widetilde{\delta t}$. The dashed line shows the best fit to $n^2 \propto \widetilde{\delta t}^{-1}$.

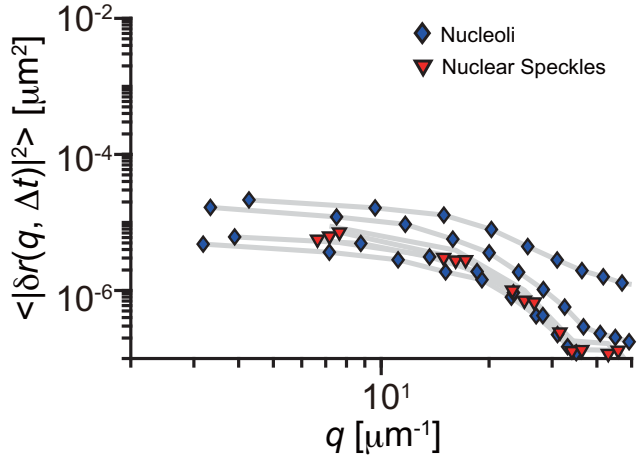

FIG. ED3. Noise floor for nucleoli and nuclear speckles. Noise floor with $\Delta t = 750$ sec for nucleoli (4 nucleoli, 2 cells) and $\Delta t = 250$ sec for nuclear speckles (3 nuclear speckles, 2 cells) after fixing the cells with 4 % paraformaldehyde.

a FUS$_N$ Corelets

	Mean-field	3D Ising
χ^2_{red}	0.87	1.94

b FUS$_N$ Corelets

	Mean-field	3D Ising
χ^2_{red}	1.8	2.5

c Nuclear Speckles

	Mean-field	3D Ising
χ^2_{red}	4.16	8.29

FIG. ED4. Chi-square values for model fits. The parameter $\chi^2_{\mathrm{red}} \gg 1$ indicates a poor model fit while $\chi^2_{\mathrm{red}} \lesssim 1$ indicates a good model fit.